Published in final edited form as:
Nat Neurosci. 2015 June ; 18(6): 883–891. doi:10.1038/nn.4015.

Spine Pruning Drives Antipsychotic-sensitive Locomotion via Circuit Control of Striatal Dopamine

Il Hwan Kim[1,8], **Mark A. Rossi**[3,7], **Dipendra K. Aryal**[4,7], **Bence Racz**[5,7], **Namsoo Kim**[3], **Akiyoshi Uezu**[1], **Fan Wang**[2], **William C. Wetsel**[1,2,4], **Richard J. Weinberg**[6], **Henry Yin**[3], and **Scott H. Soderling**[1,2,8]

[1]Departments of Cell Biology, Duke University Medical School, Durham, North Carolina.

[2]Departments of Neurobiology, Duke University Medical School, Durham, North Carolina.

[3]Departments of Psychology and Neuroscience, Duke University Medical School, Durham, North Carolina.

[4]Departments of Psychiatry and Behavioral Sciences and Mouse Behavioral and Neuroendocrine Analysis Core Facility, Duke University Medical School, Durham, North Carolina.

[5]Departments of Anatomy and Histology, Faculty of Veterinary Science, Szent István University, Budapest, Hungary.

[6]Department of Cell Biology and Physiology, and Neuroscience Center, University of North Carolina, Chapel Hill, North Carolina.

Abstract

Psychiatric and neurodevelopmental disorders may arise from anomalies in long-range neuronal connectivity downstream of pathologies in dendritic spines. However, the mechanisms that may link spine pathology to circuit abnormalities relevant to atypical behavior remain unknown. Using a mouse model to conditionally disrupt a critical regulator of the dendritic spine cytoskeleton, Arp2/3, we report here a molecular mechanism that unexpectedly reveals the interrelationship of progressive spine pruning, elevated frontal cortical excitation of pyramidal neurons, and striatal hyperdopaminergia within a cortical-to-midbrain circuit abnormality. The main symptomatic manifestations of this circuit abnormality are psychomotor agitation and stereotypical behaviors, which are relieved by antipsychotics. Moreover, antipsychotic-responsive locomotion can be directly mimicked in wildtype mice by optogenetic activation of this circuit. Collectively these

---

[8]Correspondence should be addressed to Scott H. Soderling (scott.soderling@duke.edu) and Il Hwan Kim (ilhwan.kim@duke.edu).
[7]Equal contributions.

Contributions
I.H.K. and S.H.S. designed this study. I.H.K. performed behavioral works, Golgi staining, cell biology, animal surgeries, virus infections, optical clearance of brains, immunohistochemistry, circuit tracings, and imaging. I.H.K. and W.C.W. performed pharmacology studies. I.H.K. and A.U. performed 3-D reconstruction of dendritic segments. I.H.K., F.W., and S.H.S. performed virus design and purification. N.K. and H.Y. performed whole cell patch clamp recordings. D.K.A. and W.C.W. performed HPLC and microdialysis. M.A.R. and H.Y. performed optogenetics. B.R. and R.J.W. performed electron microscopy studies. I.H.K., D.K.A., and N.K. performed statistical analyses. This paper was written by I.H.K. and S.H.S. and was edited by the other authors.

results reveal molecular and neural-circuit mechanisms, illustrating how diverse pathologies may converge to drive behaviors relevant to psychiatric disorders.

Introduction

Despite several decades of study, the mechanisms of neural circuit disturbances leading to major psychiatric symptoms remains poorly understood. Nevertheless, deciphering the circuit basis of neuropsychiatric disorders holds great potential for unifying the diverse manifestations of synaptic pathophysiology thought to lie at the root of these conditions. Moreover, distilling the polygenic basis for major psychiatric illnesses as interactions of risk alleles that alter molecular pathways important for neuronal connectivity may explain how certain risk alleles can contribute to multiple disorders[1–5].

This conceptual framing of psychiatric disorders as circuit and pathway disruptions[6] has stimulated recent analyses of genetic risk datasets for synaptic regulatory pathways that are over-represented by neuropsychiatric risk alleles. One molecular pathway notably featured by this approach is the regulation of the synaptic actin cytoskeleton[1, 7–9]. Indeed, neuropsychiatric risk genes such as *SHANK3*, *GIT1*, *DISC1*, *SRGAP3*, *OPHN1*, *LIMK1*, *NRG1*, *CYFIP1*, *SYNGAP1*, *KALRN*, and *CNKSR2* functionally orchestrate the upstream regulation of signaling events that modulate actin cytoskeletal dynamics within dendritic spines[10–21]. Dendritic spines serve as the sites for the majority of excitatory synaptic transmission in the brain; morphological abnormalities of these structures are implicated in multiple psychiatric and neurodevelopmental disorders[22, 23]. Actin dynamics within spines is intimately associated with spine morphogenesis and the efficacy of synaptic transmission[24, 25]. However, it remains unclear how disruptions of the synaptic actin cytoskeletal pathway directly relates to the synaptic pathophysiologies that result in neural circuit disturbances.

Recently, we analyzed the actin-signaling pathway in mice, testing whether the functional loss of the Arp2/3 complex in excitatory neurons of the cerebral cortex can model synaptic and behavioral phenotypes congruent to endophenotypes relevant to psychiatric disorders[25]. The Arp2/3 complex directly stimulates actin polymerization in spines downstream of synaptic activation of Rac and is composed of seven subunits[24], including the critical ArpC3 subunit that we conditionally targeted (*ArpC3*$^{f/f}$:*CaMKII*α*-Cre*, hereafter referred to as Arp2/3 mutant mice). Inhibition of this molecular pathway in cortical pyramidal neurons by deletion of ArpC3 resulted in a gradual loss of dendritic spines, and the progressive onset of behavioral abnormalities, including cognitive deficiencies, sociability deficits, reduced sensorimotor gating, and locomotor hyperactivity[25].

We report here the identification and analysis of a long-range neural circuit disturbance within the Arp2/3 mutant mice. We demonstrate that loss of Arp2/3 activity, which induces spine loss and abnormal synaptic contacts, leads to an autonomous enhancement of excitation of pyramidal cells in the frontal cortex. This abnormality results in elevated striatal dopamine (DA) and antipsychotic-responsive psychomotor disturbances, via a long-range projection to midbrain tyrosine hydroxylase (TH)-positive neurons. Together these findings demonstrate that diverse pathologies (cortical spine pruning, cortical excitation, and striatal hyperdompaminergia) can converge within a long-range circuit disturbance to trigger abnormal locomotor behavior.

Results

Arp2/3 mutant mice respond to antipsychotics

The Arp2/3 mutant mouse model progressively develops psychomotor disturbances, including locomotor hyperactivity and stereotypical activity[25]. Psychomotor behaviors in rodent models often respond to antipsychotics and are triggered by drugs that induce psychosis in humans[26]. To evaluate the Arp2/3 mutant model we therefore tested the responses of the mice to antipsychotics. In the open field test, adult mutant mice (p120–150) displayed an increased distance traveled (Fig. 1a, b), enhanced rearing (Supplementary Fig. 1a, b), and stereotypical behavior (Supplementary Fig. 1c, d), compared to their littermate controls. Consistent with prior studies[27, 28], the antipsychotic haloperidol at efficacious doses had slight sedating effects in control mice (Supplementary Fig. 1e–g). However in the Arp2/3 mutant mice, the behavioral abnormalities were dramatically reduced by haloperidol in a dose-dependent manner, and they were also significantly blunted by a 0.5mg/kg dose of the atypical antipsychotic clozapine, which showed almost no sedating effect on WT mice (Fig. 1a, b and Supplementary Fig. 1).

Antipsychotics are thought to ameliorate psychomotor symptoms largely by antagonizing effects of DA in the striatum[29], suggesting that motor disturbances in the Arp2/3 mutant mice may be due to elevated striatal DA (stDA) levels. To test this possibility, we measured the levels of DA and its metabolites within the ventral striatum of the mutant mice. High performance liquid chromatography of tissue lysates revealed significantly increased levels of DA and its metabolites, 3,4-dihydroxyphenylacetic acid (DOPAC) and homovanillic acid (HVA), in the Arp2/3 mutant striatum compared to controls. However, serotonin (5-HT) levels in the ventral striatum were unaltered in the mutant mice. These findings confirm that the motor hyperactivity of the Arp2/3 mutant mice is associated with a significant elevation of stDA.

Loss of Arp2/3 function in the mutant mice is driven by a transgene insertion of *CaMKllα* promoter-driven Cre-recombinase, which is expressed predominantly in cortical areas, with very little expression in striatum[25, 30] (Supplementary Fig. 2a–c). Consistent with this expression pattern, analyses of Arp2/3 mutant mice did not reveal morphological changes in the medium spiny neurons of the striatum (Fig. 1d, e). In contrast, the mutant mice had a 56% loss of spines in pyramidal neurons of the frontal cortex (Fig. 1f, g), which progresses over time, coincident with the appearance of hyperactivity[25]. Because haloperidol normalized hyperactivity in the mutant mice, and because this phenotype appears during a period associated with spine loss, we tested whether spine loss was reversed by acute haloperidol treatment. Reduced dendritic spine density in the frontal cortex of the Arp2/3 mutant mice was not rescued by haloperidol treatment (Supplementary Fig. 2d, e). Thus the rapid drug effect in the Arp2/3 mutant mice was not due to the morphological restoration of cortical spines, but more likely reflected the drug’s antagonism of stDA receptors. These findings led us to explore the origin of the cortical circuitry abnormalities leading to elevated stDA and its consequential behavioral outcomes.

Role of the frontal cortex in psychomotor agitation and striatal hyper-dopaminergia

To investigate a possible link between these observations in the Arp2/3 mutant model, we used a rescue approach to screen cortical areas that might be responsible for the locomotor hyperactivity and stDA. We selectively re-expressed recombinant ArpC3 in Cre-positive KO neurons within specific brain regions of the Arp2/3 mutant mice using a Flex-AAV-mediated Regional Rescue (FARR) strategy to functionally map behavioral phenotypes (Fig. 2a, b) (the selective expression of our Flex-AAV in Cre-positive cells is shown in Supplementary Fig. 3a–d). Bilateral FARR with Flex-AAV-ArpC3-2A-GFP targeting the frontal cortex significantly curtailed the locomotor hyperactivity (Fig. 2c, d), elevated rearing behavior (Fig. 2e and Supplementary Fig. 4a), and stereotypical activity (Fig. 2f and Supplementary Fig. 4b) of the Arp2/3 mutant mice. In contrast, bilateral expression of GFP (Flex-AAV-GFP) alone did not normalize these phenotypes. This effect was specific to the frontal cortex, as the same FARR strategy in the hippocampus did not rescue the motor hyperactivity of the mutant mice (Supplementary Fig. 5).

Sensory-motor gating, as assessed by pre-pulse inhibition (PPI), was previously shown to be disrupted in ArpC3 mutant mice[25]. Testing revealed that the reduced PPI in the mutant mice was not normalized by re-expression of ArpC3 within the frontal cortex (Supplementary Fig. 4c), implying that rescue of Arp2/3 in this region is not sufficient to restore normal PPI. We conclude that the frontal cortex is not the primary site important for sensory-motor gating but it is critical for the abnormal locomotor behavior seen in the Arp2/3 mutant mice.

We next asked whether the rescue of Arp2/3 function in the frontal cortex normalized the elevated stDA levels found in the Arp2/3 mutant mice. Microdialysis of the ventral striatum (Fig. 2g) revealed a ~3-fold increase in extracellular DA in the striatum of the Arp2/3 mutant mice. Importantly, DA levels were reduced by the re-expression of ArpC3 in frontal cortex, but not by GFP alone (Fig. 2h). These data support the hypothesis that loss of Arp2/3 function in frontal cortical neurons leads to abnormal behaviors through elevated DA levels in the striatum.

This possibility was further tested by unilateral rescue of the frontal cortex in Arp2/3 mutant mice, followed by monitoring for circling movement, a phenotype classically associated with imbalanced stDA levels[31]. Movement tracings of the unilaterally rescued Arp2/3 mutant mice revealed a significant rotation towards the rescued side (Fig. 2i, j). This effect was exacerbated by the psychostimulant amphetamine, which increases the DA concentration in the striatum, confirming a link between motor activity and altered stDA levels in the mutant mice (Fig. 2i, j).

Finally we specifically disrupted Arp2/3 function in the frontal cortex by infection of AAV-*CaMKII*α-Cre-GFP into the frontal cortical region of *ArpC3*$^{f/f}$ mice. Bilaterally infected mice displayed a significant increase of locomotor activity compared to those of GFP-infected littermate controls (Supplementary Fig. 6), confirming the significance of this region of cortex in controlling locomotor behaviors. Together the combined data show that Arp2/3 loss in the frontal cortex is responsible for the locomotor symptoms and is associated with elevated extracellular stDA of these mice.

Frontal cortical neurons project to dopamine neurons of the VTA/SNc

How does loss of Arp2/3 function in excitatory neurons of the frontal cortex affect stDA levels and motor behaviors? The majority of DA in the striatum is supplied by release from terminals originating from tyrosine hydroxylase (TH)-positive neurons within the ventral tegmental area/substantia nigra pars compacta (VTA/SNc). Prior studies have suggested that there is a projection from frontal cortical neurons to the VTA/SNc region[32–34]. To determine if the relevant cortical neurons of the Arp2/3 model show a similar projection, we examined the anterograde projections of frontal cortical neurons infected by the Flex-AAV-ArpC3-2A-GFP (Fig. 3a). GFP-positive axons projected ~1 cm to the VTA/SNc area (Fig. 3b). High-magnification views confirmed that axons from excitatory neurons in frontal cortex projected ventrally through the striatum, and then traversed dorsally towards TH-positive DA neurons in the VTA/SNc (Fig. 3c). Reconstructed projections from confocal z-series indicated contacts between GFP-positive frontal cortical axons and TH-positive neurons in the VTA/SNc (Fig. 3d, e). These findings suggest that the loss of Arp2/3 in the frontal cortex can directly influence DA-producing VTA/SNc neurons.

To establish the population of frontal cortical neurons that make synaptic contacts within the VTA/SNc and to directly visualize this circuit, we performed retrograde tracing of Cre-dependent GFP expression (Fig. 3f). The Cre-expressing lentiviruses were coated with rabies virus glycoprotein (Lenti-FuGB2-Cre)[35] for retrograde expression of Cre recombinase through infection of pre-synaptic terminals. We independently tested the retrograde expression of Cre by infection of the VTA/SNc region in AI-14 Cre reporter mice. tdTomato expression was readily detected in neurons that project their axons into the VTA/SNc, including medium spiny neurons in the striatum and pyramidal cells in the frontal cortex (Supplementary Fig. 7a–c), confirming the expected retrograde expression of Cre.

Using this strategy, the VTA/SNc of WT mice was infected with Lenti-FuGB2-Cre along with AAV-Flex-GFP (Cre reporter) within the frontal cortex. GFP expression in neurons of the frontal cortex marked those neurons that project their axons to neurons of the VTA/SNc that had been infected by the Lenti-FuGB2-Cre virus (Fig. 3g). Two weeks after the infection, optically cleared[36] 300 μm-thick brain sections revealed pyramidal cell bodies of GFP-positive neurons in layers 3 to 5 of the frontal cortex (Fig. 3h). High-magnification views showed axons from these pyramidal neurons directly projected to the VTA/SNc (Fig. 3i and Supplemental video 1). Confocal imaging verified that the axonal terminals of the GFP positive axons from the frontal cortex made Vglut1-positive excitatory synaptic contacts with TH-positive DA neurons within the VTA/SNc (Fig. 3j, k and Supplemental video 1). Unilateral injection of Lenti-FuGB2-Cre virus into the VTA/SNc demonstrated an ipsilateral expression of Flex-GFP within the frontal cortex, indicating that the cortical-VTA/SNc circuitry of each cortical hemisphere is independent (Supplementary Fig. 7d, e). Together these data confirm that a subpopulation of neurons in layers 3–5 of the frontal cortex provide a direct ipsilateral excitatory input to TH-positive neurons in the VTA/SNc.

Spine pruning leads to abnormal synaptic contacts in the frontal cortex

A direct excitatory pathway from the frontal cortex to the VTA/SNc implied that increased excitation of this circuit could lead to increased motor activity associated with elevated stDA levels. However our finding of a loss of dendritic spines suggested these neurons should be less excitable, due to reduced glutamatergic input. Therefore, we further examined the ultrastructural morphology of frontal cortical pyramidal neuron-synapses in the Arp2/3 mutant mice (Fig. 4a).

Transmission electron microscopic examination of randomly-selected fields confirmed the loss of spines receiving visible synaptic contacts in layers 3–5 from the Arp2/3 mutant mice (control: 32.7 ± 0.8/100 μm^2; Arp2/3 mutant: 17.2 ± 0.6/100 μm^2) (Fig. 4b). Unexpectedly, the proportion of asymmetric synapses formed directly onto dendritic shafts was greatly increased (more than five-fold) in the Arp2/3 mutant mice (control: 2.4% ± 0.5; Arp2/3 mutant: 13.8% ± 3.0) (Fig. 4b, c). Moreover, the neuropil from Arp2/3 mutant mice contained a substantial fraction of abnormal spines with short wide necks and flattened heads contacted by two spatially-separated axon terminals; these aberrant double-axon synapses were never detected in WT mice (control: 0% ± 0; mutant: 12.7% ± 2.0) (Fig. 4b, d).

In contrast, immuno-EM analysis of the GABAergic input revealed a slight but significant increase in the density of GABAergic synaptic contacts in the mutant material (control: 12.2 ± 0.5 / 100 μm^2; mutant: 14.7 ± 0.5 / 100 μm^2) in a comparable set of fields from frontal cortex (Supplementary Fig. 8). These data demonstrate that the main effect of Arp2/3 loss in cortical neuropil is on excitatory synaptic contacts, which leads to a reduction in the number of normal axonal-spine synapses. Nevertheless, axonal contacts remain, and either shift directly onto dendritic shafts or form multi-axonal synaptic contacts on the remaining spines.

Spine loss results in enhanced excitation of pyramidal neurons

Dendritic spines are thought to compartmentalize and filter synaptic input[37–39]. We hypothesized that in the absence of normal spine structures, the observed shaft and multi-axonal synapses might contribute to aberrant neuronal excitation. To test the impact of these abnormal synaptic contacts on the excitation of the cortico-VTA/SNc circuit, we selectively disrupted Arp2/3 function within this circuit to analyze synaptic physiology. The VTA/SNc of *ArpC3*$^{f/f}$ mice was infected by lenti-FuGB2-Cre viruses for retrograde expression of Cre recombinase. Cre-positive neurons within the frontal cortex (projecting to the VTA/SNc) were selectively labeled by unilateral infection with either Flex-AAV-GFP (control) or Flex-AAV-ArpC3-2A-GFP (rescue) viruses (Fig. 5a). Confocal z-series stacks of GFP-positive neurons followed by 3-D reconstruction from each side of the frontal cortex verified that there were no differences in spine densities between control KO neurons or rescued neurons at 10 days after infection (DAI) (Fig 5b, c). However, at 30 DAI, control KO neurons displayed a 53% loss of spines, compared to rescued neurons from the contralateral side (Fig 5b, c). This progressive loss of spines over time agrees with our previous report that spines are gradually lost upon Cre-mediated loss of Arp2/3 function *in vivo*[25]. This time-course provided a framework for analyzing the functional consequences of spine loss over time.

We next performed whole-cell patch clamp recordings of GFP-positive KO and rescue neurons at each time period (Fig 5d). At 10 DAI (when spine density was still normal), there were no differences in either the mEPSC amplitude or frequency (Fig. 5e–g and Supplementary Fig. 9). In contrast, at 30 DAI both mEPSC amplitude and frequency were significantly elevated in the KO neurons, compared to rescue neurons (Fig 5e–g and Supplementary Fig. 9). These findings show that the progressive loss of spines in the VTA/SNc-projecting cortical neurons is associated with the appearance of a cell-autonomous increase in neuronal excitation. This enhanced excitation may be due to the morphological abnormalities (abnormal shaft and double synapses) that emerge in response to the progressive loss of spines.

Activation of the frontal cortex to VTA/SNc circuit induces locomotion

The above behavioral, microdialysis, and electrophysiological data show that loss of Arp2/3 function triggers abnormal synaptic contacts leading to hyperactivation of a frontal cortex-to-VTA/SNc circuit. This increase in activity might ultimately drive elevated stDA and haloperidol-sensitive locomotion. Accordingly, we hypothesized that selective activation of this circuit would significantly elevate locomotor activity in WT mice, mimicking this phenotype of the Arp2/3 mutant mice. To test this hypothesis, the cortico-VTA/SNc circuit was labeled with channelrhodopsin-2 (ChR2) using a VTA/SNc lenti-FuGB2-Cre and cortical Flex-AAV-ChR2 bilateral viral infection strategy (Fig. 6a) (selective expression of Flex-AAV-ChR2-mCherry in Cre-positive cells is shown in Supplementary Fig. 3e–h). This enabled the selective activation of the circuit by optogenetic stimulation.

Stimulation of this pathway (473 nm, 10 ms square pulses; 30Hz) evoked ~2-fold elevation of locomotor activity coincident with the onset of laser stimulation (Fig. 6b–d). However, the optical activation on the same area without ChR2 (opsin-free) did not alter the activity of mice (Fig. 6c, d), confirming that acute activation stimulates movement. We next tested whether the locomotion evoked by light could be prevented by pretreatment with haloperidol, analogous to the behavioral normalization observed in the Arp2/3 mutant mice. We treated WT animals with either haloperidol (0.2 mg/kg i.p.) or vehicle 20 minutes before optogenetic stimulation. Haloperidol selectively blunted the stimulated locomotor response, compared to vehicle-treated controls (Fig. 6e, f). These results demonstrate that the excitation of the frontal cortical neurons that project to the VTA/SNc induces locomotion that is depressed by haloperidol, a DA receptor antagonist.

Activation of the frontal cortex to VTA/SNc circuit elevates striatal dopamine

To further analyze the relationship between excitation of the FC projection to the VTA/SNc and hyper-dopaminergia in the striatum, we measured extra-cellular DA in the striatum during the optogenetic activation within the VTA/SNc (Fig 6g). Two weeks after infection of the Flex-AAV-ChR2-YFP or Flex-AAV-tdTomato (opsin-free control) into the frontal cortex and Lenti-FuGB-Cre into the VTA/SNc, ChR2-YFP expression was readily found within frontal cortical pyramidal cell bodies and in their axonal fibers projecting to the VTA/SNc (Fig. 6h) (the selective expression of Flex-AAV-ChR2-YFP in Cre-positive cells is shown in Supplementary Fig. 3i–l). One week after the implantation of the probes (optogenetic and microdialysis), extracellular dialysate in the striatum was collected before and after the optogenetic stimulation (Fig. 6g). HPLC analyses revealed that an acute optogenetic stimulation of the axons in the VTA/SNc significantly increased DA, DOPAC, and HVA in the striatum compared to those of opsin-free controls (Fig. 6i). These data demonstrate that the FC-VTA/SNc projection is important for regulating DA levels in the striatum.

Together the results of the present study support a molecular and circuit-based mechanism linking cortical spine pruning to locomotor hyperactivity. Our model proposes that the progressive loss of spines in the FC caused by Arp2/3 deficiency, leads to abnormal synaptic contacts (Supplementary Fig. 10a), resulting in hyperactivation of pyramidal neurons in the frontal cortex that project to the VTA/SNc (Supplementary Fig. 10b). Enhanced activation of this circuit (Supplementary Fig. 10c–d) then produces elevated DA levels in the striatum (Supplementary Fig. 10e), which ultimately drives antipsychotic-sensitive locomotor hyperactivity (Supplementary Fig. 10f).

Discussion

The present study of Arp2/3 mutant mice follows our initial characterization of these mice, which noted that the progressive course of synaptic and behavioral phenotypes that bear similarities to symptoms associated with several psychiatric disorders, especially the cognitive, negative, and positive symptoms of schizophrenia (SZ)[25]. Disorganized behavior, which includes excessive motor activity, is a positive symptom of SZ in humans (DSM-IV-R). Motor hyperactivity and stereotypical behaviors in rodent models are considered to be relevant to the underlying neural circuit abnormalities related to the positive symptoms, because they respond well to antipsychotics and are induced by drugs that precipitate psychosis in humans[26]. Models of SZ symptoms in mice have the potential to clarify circuit-level concepts, and serve as portals to map the pathophysiology of disorder-associated symptoms. However, SZ is complicated by the observations of heterogeneous pathologies whose relationships to each other (if any) are not understood. These pathologies include excessive pruning (loss) of cortical dendritic spines, excitation of glutamatergic circuitry in the cortex, and elevated dopaminergic tone in striatum[40–42].

In this study we mapped a functional frontal cortical-VTA/SNc circuit, in which abnormal excitation emerges to drive elevated striatal dopamine levels and motor disturbances. The elevated dopamine levels and motor disturbance can be mimicked in WT animals by acute optogenetic stimulation of this pathway. Importantly, the hyperactivity of both the Arp2/3 mutant mice and optogenetically-induced mice are normalized by the antipsychotic haloperidol.

Excitatory neurons within the cortical region that make synaptic contact with the VTA/SNc appear to originate from several frontal cortical regions, including the frontal association cortex (FrA), anterior secondary motor cortex (M2), and prelimbic cortex (PrL) (for example see Supplementary Figure 11), which overlap with areas considered homologous to the primate prefrontal cortex (PFC). This long-range circuit may be conserved in humans, and functional magnetic resonance imaging suggests it functions to modulate motivation for reward in healthy individuals[43]. Synaptic refinement and maturation of the PFC continues into late childhood, suggesting disturbances within this region may correlate to the delayed onset of positive SZ symptoms[44]. Moreover, recent neuroimaging and electroencephalographic studies implicate connectivity disturbances localized to the PFC in schizophrenia[45, 46], while enhanced activation of pyramidal neurons within this region can recapitulate aspects of the disorder in rodent models[41, 47].

Our results highlight the surprising finding that loss of spines, previously observed with Golgi analysis and neuroimaging of grey matter density in many neurodevelopmental and degenerative disorders, can lead to *increased* neuronal excitation rather than decreased activation. We speculate this is most likely to occur when spine loss is triggered in postnatal periods after the formation of synapses, as opposed to impaired spine development, which can also result in reduced spine density.

Together the results of this study identify a new mechanism downstream of an impaired synaptic actin filament pathway that results in a neural circuit abnormality leading to pathological striatal dopamine and motor disturbances relevant to several psychiatric disorders. Our findings of abnormal connectivity are the first to our knowledge to provide a potential explanation for seemingly unrelated prior observations in SZ, such as pathological loss of cortical spines, enhanced excitation of cortical excitatory neurons, and altered striatal output[40–42, 48–50]. These results highlight the need for future strategies to directly target the mechanisms leading to endophenotypes relevant to psychiatric disturbance, rather than current antipsychotic drugs that appear to ameliorate the downstream consequences of circuit abnormalities.

Methods

Animals

Conditional ArpC3 knockout animals (*ArpC3$^{f/f}$*) and *CaMKIIα-Cre* line (stock# 005359; Jackson Laboratory) have been described previously[25]. The genetic background of mice was 129Sv × C57BL/6J. Male and female littermates from heterozygous pairings were used in all experiments. Rosa26-lox-stop-lox-tdTomato reporter line (generously provided by Dr. Fan Wang, Duke University, Durham, NC) and AI-14 line (B6;129S6-Gt(ROSA)26Sor$^{tm14(CAG\text{-}tdTomato)Hze}$/J; stock# 007908; Jackson Laboratory) were used for marking the Cre-positive neurons in the brain. For the optogenetic studies, C57BL/6J mice were purchased from Jackson Laboratory (stock# 000664). All mice were housed (3–5 mice per cage) in the Duke University's Division of Laboratory Animal Resources facilities (light on at 7:00AM, light off at 7:00PM). All tests were conducted during light cycle. Animal groups were randomly assigned from the animal number, and were given treatments such as viruses before testing. All procedures were conducted with a protocol approved by the Duke University Institutional Animal Care and Use Committee in accordance with National Institutes of Health guidelines.

Viruses

For production of Cre-dependent ArpC3-expressing adeno-associated virus (AAV), the ArpC3-P2A-eGFP sequence was inserted into vector backbone pAAV-EF1α-DIO (generous gift of Dr. Jonathan Ting, MIT). AAV9.EF1α.DIO.ArpC3-P2A-eGFP.WPRE (Flex-AAV-ArpC3-2A-GFP), control AAV9.EF1α.DIO.eGFP.WPRE (Flex-AAV-GFP), AAV1.EF1α.DIO.hChR2(H134R).mCherry.WPRE (Addgene20297), AAV9.EF1α.DIO.hChR2(H134R).eYFP.WPRE (Addgene20298), AAV9.CAG.Flex.tdTomato.WPRE.bGH (Allen Institute 864), AAV.9.CaMKll.HI.eGFP-Cre.WPRE, and AAV.9.hSynapsin.eGFP.RBG viruses were produced by the University of Pennsylvania Vector Core. Leni-FuGB2-Cre was described in a previous report[51]. In brief, human synapsin I (hSyn) promoter containing Cre expression vector pseudotyped lentivirus (pLV)-woodchuck posttranscriptional regulatory element (WPRE) with two helper plasmids Δ8.9 and FuGB2 (a chimeric envelope protein composed of the extracellular and transmembrane domains of rabies virus glycoprotein and the cytoplasmic domain of VSV-G; ; generously provided by Dr. Kobayashi, Fukushima Medical University, Japan)[35] were transfected into HEK293T cells using the polyethylenimine (PEI) method. Viral particles were concentrated by ultracentrifugation (82,750 × g for 2 hrs) and resuspended in PBS.

Stereotaxic surgery

For infections of viruses, mice were deeply anesthetized with intraperitoneal (i.p.) injection of ketamine (150 mg/kg) / xylazine (15 mg/kg). A 33-gauge needle was positioned in the frontal cortex (AP: +2.5, ML: +1.0, DV: −0.5 to −1.5 brain surface, relative to bregma) or into the VTA/SNc (AP: −3.5, ML: +1.0, DV: −4.2 brain surface, relative to bregma) using a stereotaxic frame (David Kopf Instruments). 0.8–1.0 μl of viruses were infused slowly over 10 min into the targets using a microdriver with a 10 μl Hamilton syringe. For rescue experiments, virus was injected into mice at p15–20 to rescue *CaMKllα-Cre* mediated deletion of ArpC3. For optogenetics, virus was injected into 6–7 week old WT mice. 2–3 weeks after viral infection, flat-cut, fiber implants (105 μm fiber diameter and 1.25 mm OD ferrule) were lowered into place bilaterally targeting the frontal cortex (AP: +2.5, ML: +1.0, DV: −0.8 brain surface, relative to bregma) and secured in place with dental acrylic.

Microdialysis and HPLC

Adult mice (p120–150) were anesthetized (i.p.) with ketamine and xylazine (80 mg/kg and 8 mg/kg, respectively), and a CMA-7 guide cannula was implanted into the right ventral striatum (AP: +1.3, ML: +1.3, DV: −3.5 brain surface, relative to bregma). Five days later a CMA-7 microdialysis probe (Cuprophane, 6kDa cut-off; 0.24 mm o.d.; 2 mm membrane length; CMA microdialysis, Kista, Sweden) was inserted into the guide cannula. Probes were perfused with artificial cerebrospinal fluid (aCSF) (in mM: 147 NaCl, 2.7 KCl, 1.2 $CaCl_2$, and 0.85 $MgCl_2$) at 0.8 μl/min. After 1h the flow-rate was reduced to 0.090 μl/min and further equilibrated for 3h before collecting the dialysate. Samples were collected into ice-cold tubes filled with 3μl of a mixture of oxalic acid, acetic acid and *l*-cysteine (1mM, 100mM, and 3mM; respectively). Samples were analyzed by HPLC-EC using an Alexys monoamine analyzer (Antec, Palm Bay, Florida, USA). The analyzer consisted of a DECADE II detector coupled to a VT-03 flow cell (Antec, USA). DA in microdialysis samples was separated on a C18 reverse-phase 1 mm×50 mm column (3 μm particle size, ALF-105; Antec, USA) at 50 μl/min using a mobile phase [50 mM phosphoric acid, 0.1 mM EDTA, 8 mM KCl, 12% methanol, and 500 mg/L 1-octane sulfonic acid sodium salt, pH 6.0] at a potential of 0.3 volts. The chromatograms were analyzed using the Clarity software package (DataApex, Prague, Czech Republic) where a signal-to-noise ratio (SNR) of 3 was considered the limit of detection. For simultaneous optogenetic and microdialysis experiments, microdialysis was performed using bilateral cannulation (AP: +1.3, ML: ±1.3, DV: −3.5 brain surface, relative to bregma). Probes were perfused with aCSF (1.2 μl/min) and equilibrated for an hour before collecting first baseline samples and then laser-stimulated samples. All samples were collected and analyzed as above. To measure levels of DA and its metabolites in tissue, ventral striatum was rapidly dissected, flash frozen in liquid nitrogen, and stored at −80°C until analysis. Dopamine and its metabolites were measured in a Coulochem III HPLC system with 5014B analytical cell and 5020 guard cell (ESA Inc., Chelmsford, MA, USA). The guard cell potential was set at +0.38 mV and the first and second electrodes of the analytical cell were at −0.15 and +0.35 mV, respectively. All quantifications were conducted in a blinded manner.

Imaging

All representative images were from at least 3 samples.

Golgi-Cox staining

Golgi-Cox staining procedures were performed as previously described[25, 52, 53]. Adult mice (p120–150) were deeply anesthetized with isoflurane and then perfused transcardially with Tris-buffered saline (TBS; pH 7.4) containing 25 U/ml heparin, followed by 4% paraformaldehyde (PFA) in TBS. Brains were removed and treated with solutions A and B from the FD Rapid GolgiStain Kit (FD NeuroTechnologies) for 2 weeks and then treated with solution C for 7 days. Sections (100 μm thick) were cut by cryostat and transferred to solution C and incubated for 24 hrs at 4°C. After rinsing briefly with distilled water, floating sections were stained with solutions D and E for 30 min and then transferred to a 0.05% gelatin solution. Sections were mounted onto glass slides, dehydrated through a graded series of ethanol concentrations, and then mounted with Permount® (Fisher Scientifics). Z-series images of secondary or tertiary branches of neurons were collected on an AxioCam MRm (Zeiss) on an Axio Imager M1 microscope (Zeiss) under a 63× oil-immersion objective using AxioVision 4.8.2 software (Zeiss). For quantification, spine density was calculated from the Z-series images of pyramidal neurons from the frontal cortex (layers 3–5) or striatal medium spiny neurons using ImageJ software (NIH). All quantifications were conducted in a blinded manner.

Circuit tracing

Mice infected with Flex-AAV-ArpC3-2A-GFP within the frontal cortex at p15–20 were perfused at p120–150 as described above. Brains were removed, post-fixed overnight at 4°C, and then cryo-protected with 30% sucrose in TBS. Brains were cut into 50 μm sagittal sections by cryostat (Leica CM 3000). Sections were treated with blocking solution (TBS containing 5% normal goat serum and 0.2% Triton X-100) for 2 hr and incubated overnight at 4°C with rabbit anti-tyrosine hydroxylase polyclonal antibody (1:1,000; Calbiochem; Cat# 657012). After washing three times for 10 min per wash with TBST (TBS containing 0.2% Triton X-100), sections were incubated with Alexa Fluor® 555 IgG (1:500; Molecular Probes) for 1 hr at room temperature. Sections were counterstained with a 4',6-diamidino-2-phenylindole solution (DAPI; Sigma-Aldrich). After washing four times, the sections were coverslipped with FluorSave (CalBioChem) aqueous mounting medium. Sagittal images were taken by tile scan imaging using LSM 710 confocal microscope (Zeiss).

For the axonal fiber tracing, adult WT mice (2–3 months old) were infected with Lenti-FuGB2-Cre (VTA/SNc) and AAV-Flex-GFP (frontal cortex) for two weeks. The perfused/cryoprotected brains were cut into 300 μm sagittal sections using a cryostat (Leica CM 3000), and then optically cleared by the SeeDB method as described[36]. Whole sagittal image were taken by tile scan imaging using a LSM 710 confocal microscope (Zeiss) with a 10× objective under control of Zen software (Zeiss). For triple labeling, sagittal brain sections (50 μm thick) were incubated overnight at 4°C with guinea pig anti-Vglut1 antibody (1:500; Millipore; Cat# AB5905) together with rabbit anti-tyrosine hydroxylase polyclonal antibody (1:1,000). After washing, sections were incubated with anti-guinea pig Alexa Fluor® 647 IgG (1:100; Molecular Probes) and anti-rabbit Alexa Fluor® 555 IgG (1:500; Molecular Probes). Immunostaining was conducted as described above. The z-series images were acquired on a LSM 710 confocal microscope (Zeiss) and 3-D reconstructed using Imaris software (Bitplane).

Dendritic spine analysis

3-D reconstructions of dendritic segments using confocal images were performed as previously described[25]. Briefly, perfused/cryoprotected brains were cut into 40 μm sagittal sections by cryostat (Leica CM 3000). Images of dendritic spines from secondary or tertiary branches of pyramidal neurons in layers 3–5 of frontal cortex were taken on a LSM 710 confocal microscope (Zeiss). All images were acquired by z-series (0.13 μm intervals) using a 63× oil-immersion objective. The z-series of images were deconvolved by Huygens Essential deconvolution software (SVI) and then 3-D reconstructed and measured by Imaris software (Bitplane). All quantifications were conducted in a blinded manner.

Transmission electron microscopy

Experiments were carried out as described[25] on 4–5 months old *ArpC3*$^{f/f}$*:CaMKIIαCre* mice and their littermate controls (*ArpC3*$^{f/f}$) (n=3 for both groups). Animals were deeply anesthetized with pentobarbital (60 mg/kg, i.p.), then perfused intracardially with saline, followed by a mixture of depolymerized paraformaldehyde (4%) and glutaraldehyde (0.2 – 2%) in 0.1 M phosphate buffer pH 7.4 (PB). Brain tissue containing the frontal cortex was postfixed in 0.5–1% osmium tetroxide in 0.1 M PB for 35–45 min and stained *en bloc* with 1% uranyl acetate for 1 h. After dehydration in ascending ethanol series and propylene oxide, sections from layers 3–5 of frontal cortex were infiltrated with Epon/Spurr resin (EMS) and flat-mounted between sheets of Aclar within glass slides. For single section analysis, 70 nm sections were cut and mounted on 300 mesh copper grids; for three-dimensional reconstruction 60 nm serial sections were mounted on formvar-coated single slot nickel grids (EMS) and contrasted with stabilized 3% lead citrate (Ultrostain 2, Leica).

For postembedding GABA immunoreaction, thin (~100 nm) sections were collected on nickel mesh grids and processed for immunogold labeling. Briefly, after treatment at 60° C with 0.01 M citrate buffer followed by a short incubation in 0.02 M Tris-buffered saline containing 0.005% NP-10 detergent, pH 7.6 (TBSN), grids were incubated overnight at

37°C with the primary antibody (polyclonal rabbit anti-GABA, Sigma, Cat# A-2052). Grids were then transferred to TBSN, pH 7.6, incubated for 1 hr in the secondary antibody (goat anti-rabbit conjugated to 20 nm gold particles (1:15 in TBSN, pH 8.2; British BioCell; Ted Pella, Redding, CA, cat# 15728), and counterstained with uranyl acetate and Sato's lead. When primary antiserum was omitted as a control, virtually no gold particles could be detected on the sections.

Material was examined in a JEOL T1011 electron microscope at 80 KV; randomly-selected images from single sections were collected with a MegaView (Soft Imaging System) 12 bit 1024×1024 CCD camera at uniform magnification, examining dendritic spines (as defined by the presence of a clearly visible synaptic cleft and a postsynaptic density in the spine), and synaptic contacts to pyramidal cell shafts; results were generally consistent among animals. We used the freely available Reconstruct software (see http://synapses.clm.utexas.edu/tools/reconstruct/reconstruct.stm) to reconstruct spines from serial sections. All quantifications were conducted in a double-blinded manner.

Whole-cell patch clamp recording

For whole-cell patch-clamp recordings, brains from animals (infected at p40–60) (WT, n=9; cKO-30 days, n=15 pairs of hemispheres for each group; cKO-10 days, n=10 pairs of hemispheres for each group) were removed quickly into ice-cold solution bubbled with 95% O_2-5% CO_2 containing the following (in mM): 194 sucrose, 30 NaCl, 2.5 KCl, 1 $MgCl_2$, 26 $NaHCO_3$, 1.2 NaH_2PO_4, and 10 D-glucose. After 5 minutes the brains were blocked and coronal slices were taken at 200 μm. During the recovery period (30 minutes), slices were incubated at 35.5°C with oxygenated aCSF solution containing the following (in mM): 124 NaCl, 2.5 KCl, 2 $CaCl_2$, 1 $MgCl_2$, 26 $NaHCO_3$, 1.2 NaH_2PO_4, and 10 *D*-glucose. Pipettes (2.5–5 MΩ) contained the following (in mM): 120 cesium methane sulfonate, 5 NaCl, 10 tetraethylammonium chloride, 10 HEPES, 4 lidocaine N-ethyl bromide, 1.1 EGTA, 4 magnesium ATP, and 0.3 sodium GTP, pH adjusted to 7.2 with CsOH and osmolality set to ~300 mosM with sucrose.

Recordings were performed with a MultiClamp 700B amplifier (Molecular Device). Signals were filtered at 10 kHz and digitized at 20 kHz with a Digidata 1440A digitizer (Molecular Devices). Slices were maintained under continuous perfusion of aCSF at 28–29°C with a 2–3 ml/min flow rate. In the whole-cell configuration (series resistance < 20 MΩ), we recorded miniature EPSCs (mEPSCs) on the cell bodies of GFP-positive neurons with 50μM picrotoxin and 2μM tetrodotoxin (TTX) in the bath solution in voltage-clamp mode (cells held at −70 mV). The amplitudes and frequencies of mEPSCs were analyzed using peak detection software in pCLAMP10 (Molecular Devices). All recordings were conducted such that the experimenter was blinded to each group.

Optogenetics

Optogenetic experiments were conducted as described[54]. Testing began at least one week after implant surgery. On test days, mice were lightly anesthetized with isoflurane and then connected to a 473-nm DPSS laser (Shanghai Laser & Optics) via 62.3 μm core diameter sheathed fibers, connected to the implant with ceramic ferrule sleeves. A single laser beam was split (50:50) with a 1×2 optical commutator (Doric) to deliver ~5mW optical power to each hemisphere. Testing took place in a cylindrical chamber (18 cm diameter). Videos were captured from directly above at 30 fps. Stimulation was delivered for 2 minutes (10 ms square pulses; 30Hz). For drug testing, haloperidol (0.2 mg/kg i.p.) or vehicle (saline) was injected 20 min before laser stimulation. Data are presented as the proportion of distance traveled during the ten minutes prior to laser stimulation. The position of each mouse was tracked frame-by-frame offline using custom tracking software (MatLab). Position data were used to calculate the distance traveled in one-minute bins throughout the session.

For simultaneous microdialysis and optogenetic experiments, optic fibers were placed bilaterally over the VTA (AP −3.5, ML +1.2, DV 4.0). Prior to testing, mice were lightly anesthetized with isoflurane and connected to the laser and microdialysis probes were inserted. Stimulation (2 min duration; 10 ms square pulses; 30Hz) was delivered after achieving equilibrium and collecting baseline samples. All experiments were conducted in a blinded manner.

Behavioral tests

Viruses were stereotaxically injected at p15–20. All behavioral tests were conducted during light cycle at p90–120. Mice showing seizure behaviors were excluded from behavioral tests. Experimenter was blinded to genotypes and drug treatments.

Open field activity

Mice were placed into a square (21 cm×21 cm) open field (AccuScan Instruments) and their motor activities were monitored for over 1 hr under a 350 lux illumination using VersaMax software (AccuScan Instruments). In experiments with antipsychotics, baseline activity was monitored for 1 hr, mice were injected (i.p.) with vehicle or drugs (0.1 or 0.2 mg/kg haloperidol or 0.5 mg/kg clozapine), and were returned immediately to the open field for 2 hrs. Locomotor (distance traveled), rearing (vertical beam-breaks), and stereotypical activities (repetitive beam-breaks <1 sec) were measured in 5-min time-bins.

Circling motor activity

One μl of Flex-AAV-GFP (control) and Flex-AAV-ArpC3-2A-GFP (rescue) were stereotaxically injected into each side of frontal cortex (random order). Mice were placed into a large open field (42 cm×42 cm; AccuScan Instruments) to measure motor activity at p120–150. The baseline rotational locomotion was monitored by VersaMax software (AccuScan Instruments) for 30 min, and then the mice were injected (i.p.) with amphetamine (2.0 mg/kg), and were returned to the open field for further movement tracing for 1 hr.

Pre-pulse inhibition (PPI)

PPI of the acoustic startle response was measured with SDI equipment as described[25]. After 5 min of acclimation to the apparatus, mice were given three different types of trials: trials with the startle stimulus only (40 ms 120 dB); trials with the prepulse stimuli (20 ms) that were 4, 8, or 12 dB above the white-noise background (64 dB) and followed 100 msec later with the startle stimulus; and trials with background stimuli (null trials) to control for background movements of the animals. Each test session began with 7 startle trials, followed by blocks of 5 null, 15 prepulse, and 9 startle trials presented in a pseudorandom order, and ending with 5 startle trials. The average inter-trial interval was 15 sec, with a range of 12 to 30 sec. The peak startle responses for each trial were measured between 35 and 65 ms after the onset of the startle stimulus. PPI was calculated as %PPI = [1 − (prepulse trials/startle-only trials)]*100. The magnitude of the startle response was calculated as the mean response from all trials, excluding the initial block or 7 and final block of 5 trails.

Statistical analyses

All statistical tests used in this study were performed two-sided. All data are expressed as means ± SEM and all statistics were analyzed using SPSS 20.0 (IBM). Independent *t*-tests were used for analysis of differences between two groups. When comparing more than two groups ANOVA were used followed by Bonferroni corrected pair-wise comparisons. To monitor changes over time, repeated-measures ANOVA were run followed by Bonferroni corrected pair-wise comparisons. A $p<0.05$ was considered statistically significant. None of the data points were excluded from analyses. Data distribution was assumed to be normal but this was not formally tested. No statistical methods were used to predetermine sample sizes but our sample sizes are similar to those reported in previous publications. Detailed information on the statistical methods and results can be found in Supplementary Table 1.

Supplementary Material

Refer to Web version on PubMed Central for supplementary material.

Acknowledgements

We thank Drs. Marc Caron, Brigid Hogan, and Cagla Eroglu for their critical reading and comments. We also thank Dr. Katsuyasu Sakurai for providing the modified FuGB2 viral vector, and thank Dr. Ramona Rodriguiz and Erin Spence for behavioral technical support. This work was supported by the following grants: NIH MH103374 and NS059957 (SHS), NIH NS077986 (FW), AA021074 (HY), NS039444 (RJW), and MH082441 (WCW). MR is supported by an NSF fellowship and BR is supported by the János Bólyai Research Fellowship from the Hungarian Academy of Sciences, by the Hungarian Scientific Research Fund (OTKA, grant #K83830), and also by the Research Faculty Grant 2014 of the Szent István University, Faculty of Veterinary Science. Some of the experiments were conducted with equipment/software purchased with a North Carolina Biotechnology Center grant (WCW).

References

1. Purcell SM, et al. A polygenic burden of rare disruptive mutations in schizophrenia. Nature. 2014; 506:185–190. [PubMed: 24463508]
2. Lee SH, et al. Estimating the proportion of variation in susceptibility to schizophrenia captured by common SNPs. Nat Genet. 2012; 44:247–250. [PubMed: 22344220]
3. Malhotra D, Sebat J. CNVs: harbingers of a rare variant revolution in psychiatric genetics. Cell. 2012; 148:1223–1241. [PubMed: 22424231]
4. Stergiakouli E, et al. Investigating the contribution of common genetic variants to the risk and pathogenesis of ADHD. Am J Psychiatry. 2012; 169:186–194. [PubMed: 22420046]
5. McCarroll SA, Hyman SE. Progress in the genetics of polygenic brain disorders: significant new challenges for neurobiology. Neuron. 2013; 80:578–587. [PubMed: 24183011]
6. Hyman SE. Perspective: Revealing molecular secrets. Nature. 2014; 508:S20. [PubMed: 24695333]
7. Fromer M, et al. De novo mutations in schizophrenia implicate synaptic networks. Nature. 2014; 506:179–184. [PubMed: 24463507]

8. Kirov G, et al. De novo CNV analysis implicates specific abnormalities of postsynaptic signalling complexes in the pathogenesis of schizophrenia. Mol Psychiatry. 2012; 17:142–153. [PubMed: 22083728]
9. Chang J, Gilman SR, Chiang AH, Sanders SJ, Vitkup D. Genotype to phenotype relationships in autism spectrum disorders. Nat Neurosci. 2014
10. Han K, et al. SHANK3 overexpression causes manic-like behaviour with unique pharmacogenetic properties. Nature. 2013; 503:72–77. [PubMed: 24153177]
11. Durand CM, et al. SHANK3 mutations identified in autism lead to modification of dendritic spine morphology via an actin-dependent mechanism. Mol Psychiatry. 2012; 17:71–84. [PubMed: 21606927]
12. Won H, et al. GIT1 is associated with ADHD in humans and ADHD-like behaviors in mice. Nat Med. 2011; 17:566–572. [PubMed: 21499268]
13. Hayashi-Takagi A, et al. Disrupted-in-Schizophrenia 1 (DISC1) regulates spines of the glutamate synapse via Rac1. Nat Neurosci. 2010; 13:327–332. [PubMed: 20139976]
14. Carlson BR, et al. WRP/srGAP3 facilitates the initiation of spine development by an inverse F-BAR domain, and its loss impairs long-term memory. J Neurosci. 2011; 31:2447–2460. [PubMed: 21325512]
15. Govek EE, et al. The X-linked mental retardation protein oligophrenin-1 is required for dendritic spine morphogenesis. Nat Neurosci. 2004; 7:364–372. [PubMed: 15034583]
16. Meng Y, et al. Abnormal spine morphology and enhanced LTP in LIMK-1 knockout mice. Neuron. 2002; 35:121–133. [PubMed: 12123613]
17. Gu Z, Jiang Q, Fu AK, Ip NY, Yan Z. Regulation of NMDA receptors by neuregulin signaling in prefrontal cortex. J Neurosci. 2005; 25:4974–4984. [PubMed: 15901778]
18. De Rubeis S, et al. CYFIP1 coordinates mRNA translation and cytoskeleton remodeling to ensure proper dendritic spine formation. Neuron. 2013; 79:1169–1182. [PubMed: 24050404]
19. Clement JP, et al. Pathogenic SYNGAP1 mutations impair cognitive development by disrupting maturation of dendritic spine synapses. Cell. 2012; 151:709–723. [PubMed: 23141534]
20. Russell TA, et al. A sequence variant in human KALRN impairs protein function and coincides with reduced cortical thickness. Nat Commun. 2014; 5:4858. [PubMed: 25224588]
21. Vaags AK, et al. Absent CNKSR2 causes seizures and intellectual, attention, and language deficits. Ann Neurol. 2014; 76:758–764. [PubMed: 25223753]
22. Koleske AJ. Molecular mechanisms of dendrite stability. Nat Rev Neurosci. 2013; 14:536–550. [PubMed: 23839597]
23. Penzes P, Cahill ME, Jones KA, VanLeeuwen JE, Woolfrey KM. Dendritic spine pathology in neuropsychiatric disorders. Nat Neurosci. 2011; 14:285–293. [PubMed: 21346746]
24. Mullins RD, Stafford WF, Pollard TD. Structure, subunit topology, and actin-binding activity of the Arp2/3 complex from Acanthamoeba. J Cell Biol. 1997; 136:331–343. [PubMed: 9015304]
25. Kim IH, et al. Disruption of Arp2/3 results in asymmetric structural plasticity of dendritic spines and progressive synaptic and behavioral abnormalities. J Neurosci. 2013; 33:6081–6092. [PubMed: 23554489]
26. van den Buuse M. Modeling the positive symptoms of schizophrenia in genetically modified mice: pharmacology and methodology aspects. Schizophr Bull. 2010; 36:246–270. [PubMed: 19900963]
27. Mohn AR, Gainetdinov RR, Caron MG, Koller BH. Mice with reduced NMDA receptor expression display behaviors related to schizophrenia. Cell. 1999; 98:427–436. [PubMed: 10481908]
28. Hoffman DC, Donovan H. Catalepsy as a rodent model for detecting antipsychotic drugs with extrapyramidal side effect liability. Psychopharmacology (Berl). 1995; 120:128–133. [PubMed: 7480543]
29. Creese I, Burt DR, Snyder SH. Dopamine receptor binding predicts clinical and pharmacological potencies of antischizophrenic drugs. Science. 1976; 192:481–483. [PubMed: 3854]
30. Tsien JZ, et al. Subregion- and cell type-restricted gene knockout in mouse brain. Cell. 1996; 87:1317–1326. [PubMed: 8980237]

31. Ungerstedt U, Arbuthnott GW. Quantitative recording of rotational behavior in rats after 6-hydroxy-dopamine lesions of the nigrostriatal dopamine system. Brain Res. 1970; 24:485–493. [PubMed: 5494536]
32. Watabe-Uchida M, Zhu L, Ogawa SK, Vamanrao A, Uchida N. Whole-brain mapping of direct inputs to midbrain dopamine neurons. Neuron. 2012; 74:858–873. [PubMed: 22681690]
33. Sesack SR, Pickel VM. Prefrontal cortical efferents in the rat synapse on unlabeled neuronal targets of catecholamine terminals in the nucleus accumbens septi and on dopamine neurons in the ventral tegmental area. J Comp Neurol. 1992; 320:145–160. [PubMed: 1377716]
34. Parker JG, Beutler LR, Palmiter RD. The contribution of NMDA receptor signaling in the corticobasal ganglia reward network to appetitive Pavlovian learning. J Neurosci. 2011; 31:11362–11369. [PubMed: 21813695]
35. Kato S, et al. A lentiviral strategy for highly efficient retrograde gene transfer by pseudotyping with fusion envelope glycoprotein. Hum Gene Ther. 2011; 22:197–206. [PubMed: 20954846]
36. Ke MT, Fujimoto S, Imai T. SeeDB: a simple and morphology-preserving optical clearing agent for neuronal circuit reconstruction. Nat Neurosci. 2013; 16:1154–1161. [PubMed: 23792946]
37. Harnett MT, Makara JK, Spruston N, Kath WL, Magee JC. Synaptic amplification by dendritic spines enhances input cooperativity. Nature. 2012; 491:599–602. [PubMed: 23103868]
38. Tonnesen J, Katona G, Rozsa B, Nagerl UV. Spine neck plasticity regulates compartmentalization of synapses. Nat Neurosci. 2014; 17:678–685. [PubMed: 24657968]
39. Yuste R. Electrical compartmentalization in dendritic spines. Annu Rev Neurosci. 2013; 36:429–449. [PubMed: 23724997]
40. Laruelle M, et al. Single photon emission computerized tomography imaging of amphetamine-induced dopamine release in drug-free schizophrenic subjects. Proc Natl Acad Sci U S A. 1996; 93:9235–9240. [PubMed: 8799184]
41. Belforte JE, et al. Postnatal NMDA receptor ablation in corticolimbic interneurons confers schizophrenia-like phenotypes. Nat Neurosci. 2010; 13:76–83. [PubMed: 19915563]
42. Gainetdinov RR, Mohn AR, Caron MG. Genetic animal models: focus on schizophrenia. Trends Neurosci. 2001; 24:527–533. [PubMed: 11506886]
43. Ballard IC, et al. Dorsolateral prefrontal cortex drives mesolimbic dopaminergic regions to initiate motivated behavior. J Neurosci. 2011; 31:10340–10346. [PubMed: 21753011]
44. Insel TR. Rethinking schizophrenia. Nature. 2010; 468:187–193. [PubMed: 21068826]
45. Lawrie SM, et al. Reduced frontotemporal functional connectivity in schizophrenia associated with auditory hallucinations. Biol Psychiatry. 2002; 51:1008–1011. [PubMed: 12062886]
46. Ford JM, Mathalon DH, Whitfield S, Faustman WO, Roth WT. Reduced communication between frontal and temporal lobes during talking in schizophrenia. Biol Psychiatry. 2002; 51:485–492. [PubMed: 11922884]
47. Yizhar O, et al. Neocortical excitation/inhibition balance in information processing and social dysfunction. Nature. 2011; 477:171–178. [PubMed: 21796121]
48. Sun D, et al. Progressive brain structural changes mapped as psychosis develops in 'at risk' individuals. Schizophr Res. 2009; 108:85–92. [PubMed: 19138834]
49. McIntosh AM, et al. Longitudinal volume reductions in people at high genetic risk of schizophrenia as they develop psychosis. Biol Psychiatry. 2011; 69:953–958. [PubMed: 21168123]
50. Glausier JR, Lewis DA. Dendritic spine pathology in schizophrenia. Neuroscience. 2013; 251:90–107. [PubMed: 22546337]

References

51. Nelson A, et al. A circuit for motor cortical modulation of auditory cortical activity. J Neurosci. 2013; 33:14342–14353. [PubMed: 24005287]
52. Kim IH, Wang H, Soderling SH, Yasuda R. Loss of Cdc42 leads to defects in synaptic plasticity and remote memory recall. Elife. 2014; 3

53. Kim IH, et al. Inositol 1,4,5-trisphosphate 3-kinase a functions as a scaffold for synaptic Rac signaling. J Neurosci. 2009; 29:14039–14049. [PubMed: 19890013]

54. Rossi MA, et al. Prefrontal cortical mechanisms underlying delayed alternation in mice. J Neurophysiol. 2012; 108:1211–1222. [PubMed: 22539827]

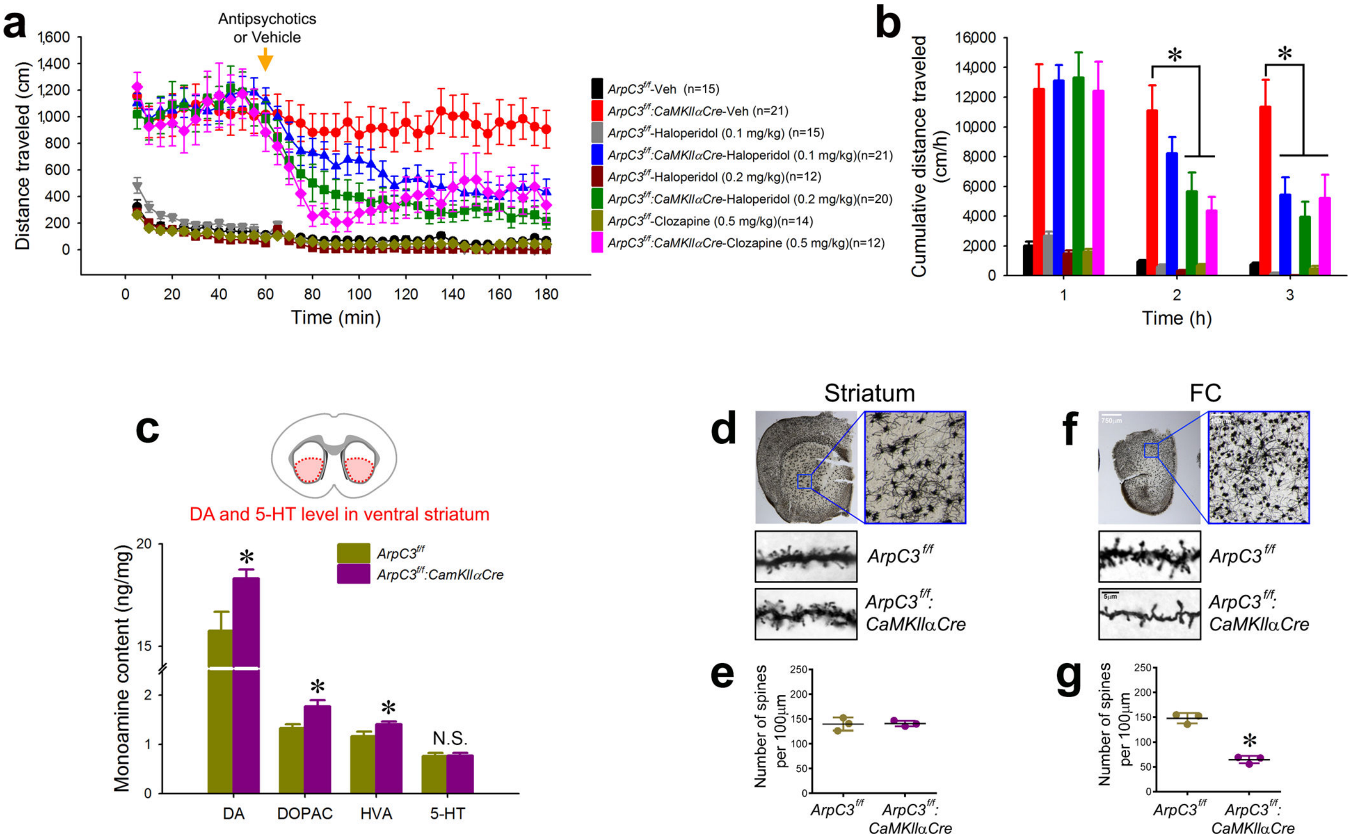

Fig. 1. Arp2/3 mutant mice respond to antipsychotics and exhibit elevated striatal dopamine

(**a**) Open field analysis of locomotor activity over time for Arp2/3 mutant (*ArpC3*$^{f/f}$*:CaMKIIαCre*) or control (*ArpC3*$^{f/f}$) mice given an (i.p.) vehicle (saline) or drug (haloperidol or clozapine) at 60 min (arrow) (n=12–21). (**b**) Cumulative distance moved per hour for each condition from (a). (**ps*<0.05; two-way repeated-measures ANOVA followed by *post-hoc* tests) (**c**) HPLC-EC analysis of dopamine (DA) and its metabolites [3,4-dihydroxypheylacetic acid (DOPAC) and homomovanallic acid (HVA)], and serotonin (5-HT) from the ventral striatum of Arp2/3 mutant (n=7) and control mice (n=6) (**ps*<0.05; independent *t*-tests). (**d** to **g**) Golgi stain analysis of dendritic spine density from the ventral striatum (d & e) and frontal cortex (FC) (f & g) of Arp2/3 mutant and control mice (n=3 for each group). Representative images (d & f) and average density (e & g) are shown (**p*<0.001; independent *t*-test). Data are presented as mean ±SEM.

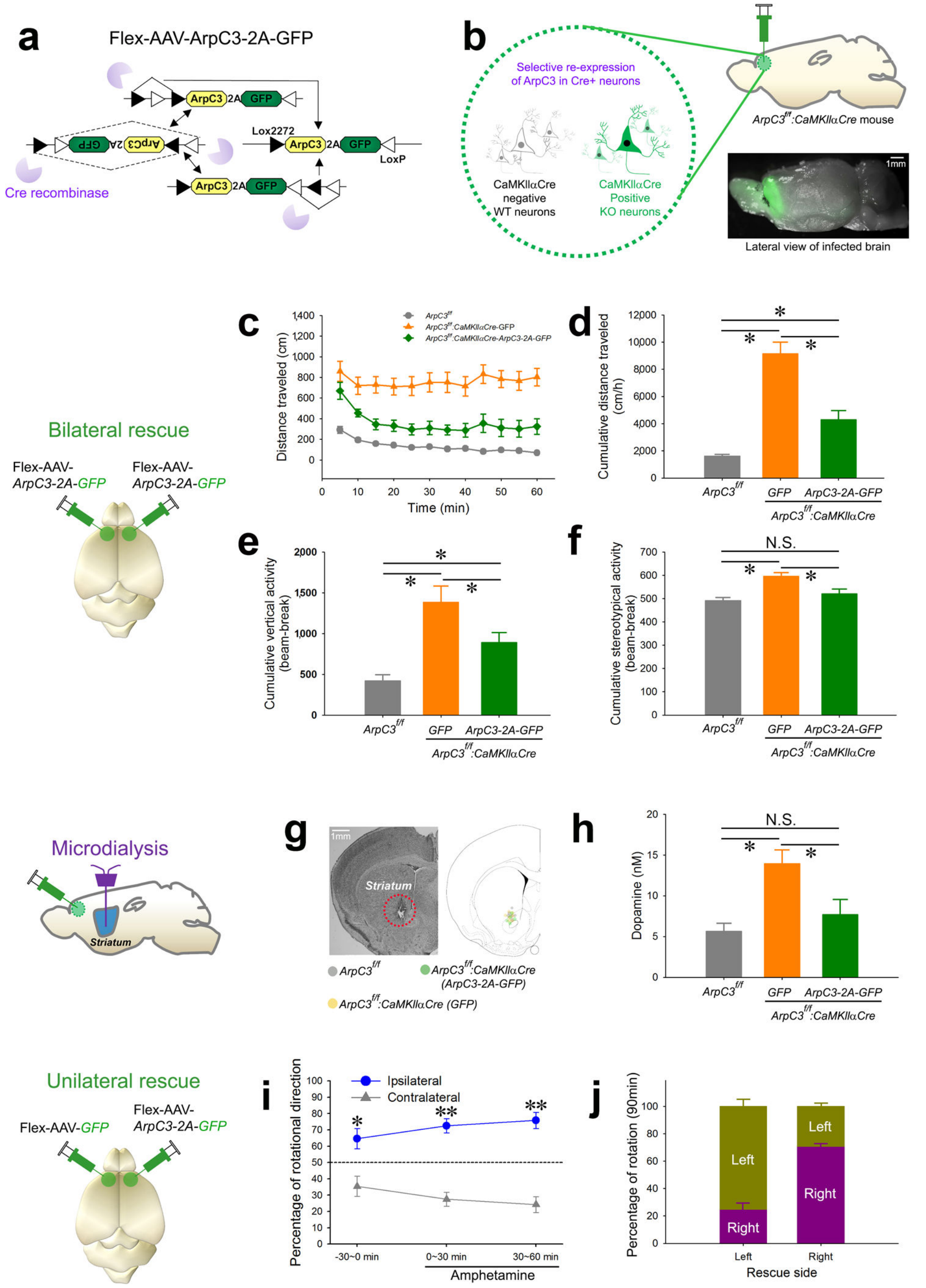

Fig. 2. Regional rescue implicates the frontal cortex in mediating the elevated motor activity and striatal dopaminergic tone of the Arp2/3 mutant mice

(**a**) Schematic representation of the Cre-dependent ArpC3-expressing rescue adeno-associated virus (AAV). (**b**) Illustration representing the selective re-expression of ArpC3 and GFP in *CaMKIIαCre* positive neurons. Bottom image shows the extent of expression in forebrain from a single injection. (**c** to **f**) Analysis of open field activity following bilateral rescue of Arp2/3 activity in the frontal cortex. (**c**) Mean distance traveled every 5 min for *ArpC3*$^{f/f}$(WT) (gray line; n=18), *ArpC3*$^{f/f}$:*CaMKIIαCre*-GFP (cKO-control; bilateral GFP virus) (orange line; n=11), and *ArpC3*$^{f/f}$:*CaMKIIαCre*-ArpC3 (cKO-rescue; bilateral ArpC3 virus) (green line; n=15) mice. (**d**) Cumulative distance (**p*<0.01), (**e**) vertical activity (**p*<0.05), and (**f**) stereotypical (**p*<0.05) behavior for WT (gray bar), cKO-control (orange bar), and cKO-rescue (green bar) mice (One-way ANOVAs followed by post-hoc tests). (**g**) Representative image shows the placement of microdialysis probes. (**h**) Mean extracellular levels of dopamine in ventral striatum of WT (gray bar; n=6), cKO-control (orange bar; n=6), and cKO-rescue mice (green bar; n=6) (**p*s<0.05; one-way ANOVA followed by *post-hoc* tests). (**i**) Plot of percent rotational movement for 30 min ipsilateral (blue line) versus contralateral (gray line) to the unilateral rescue of ArpC3 in the Arp2/3 mutant mice (n=7) before (−30 min) (**p*<0.005) and after amphetamine injection (0–30 and 30–60 min) (***ps*<0.0001). (**j**) Percentage of rotational movement for either left or right FC rescue mice for 90 min. All data are presented as mean ±SEM.

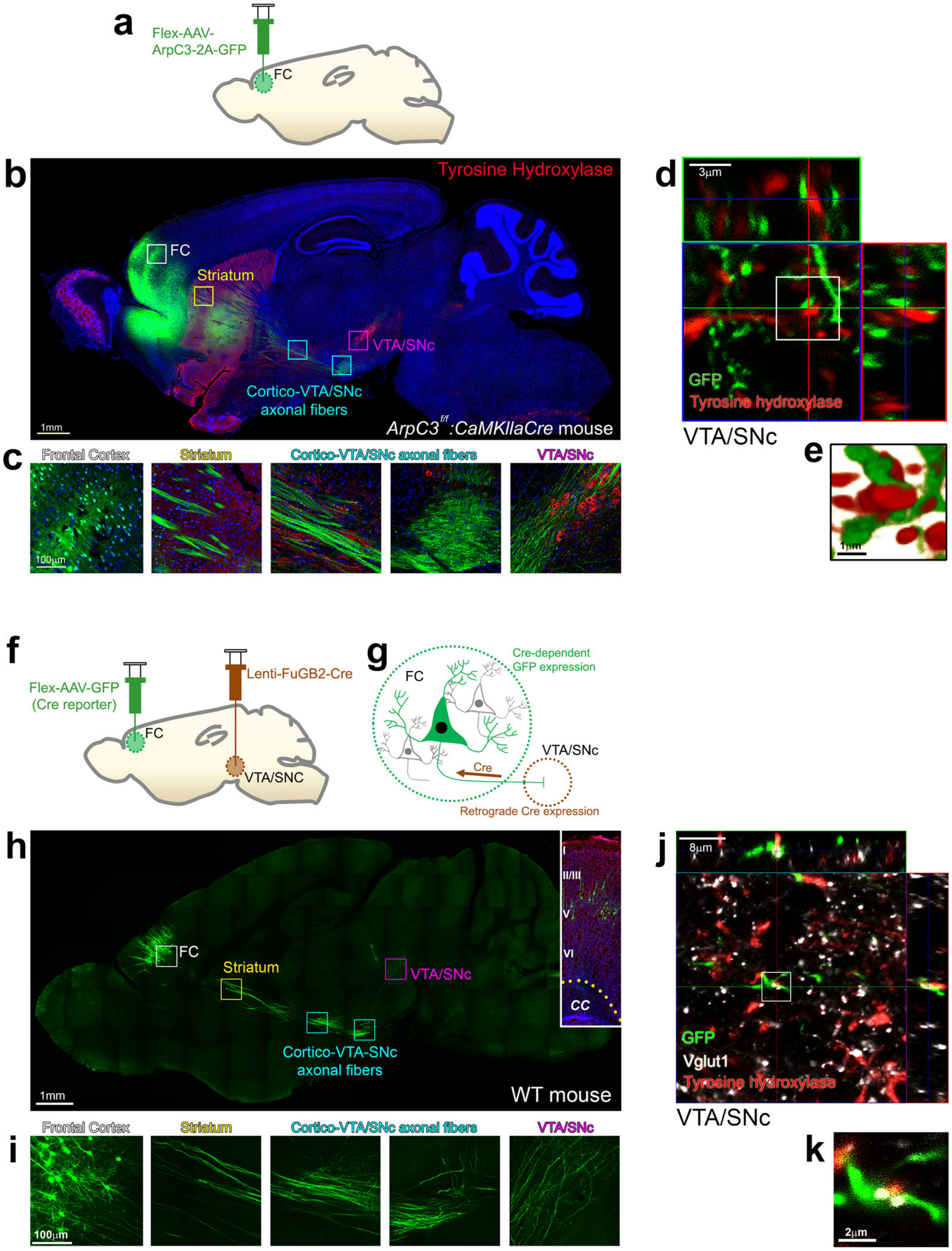

Fig. 3. Arp2/3 rescued excitatory neurons of the frontal cortex project to and make synaptic contacts within the VTA/SNc

(**a**) Schematic representation of the rescue virus (Flex-AAV-ArpC3-2A-GFP) injection into the frontal cortex (FC). (**b**) Representative sagittal section image of GFP (green) expression and immunostaining for tyrosine hydroxylase (red) from an Arp2/3 frontal cortical rescue mouse. Boxes represent higher magnification images in (**c**). (**c**) High magnification images tracing the GFP positive neurons and their afferents from the FC all the way to the ventral tegmental area (VTA)/substantia nigra (SNc). (d) Representative maximum projection image with orthogonal views of GFP positive axons (green) and tyrosine hydroxylase immunohistochemistry (red) within the VTA/SNc. GFP within axons is from an *ArpC3*$^{f/f}$: *CaMKIIαCre* mouse with Flex-AAV-ArpC3-2A-GFP virus injected into the FC. (**e**) High magnification surface rendering depicting contact between FC axons and tyrosine hydroxylase positive neurons within the VTA/SNc. (**f** and **g**) Schematic representation of the retrograde viral tracing between the VTA/SNc and FC. (**h**) Representative sagittal section visualizing Cre-dependent GFP expression in the FC mediated by a Cre-expressing rabies/lenti-viral injection (Lenti-FuGB2-Cre) into the VTA/SNc. Boxes represent higher magnification images in (i). Inset shows GFP-positive neurons from a FC section stained with DAPI (blue) and NeuroTrace® (red) to visualize the cortical layers. *CC*, corpus callosum. (**i**) High magnification images tracing the GFP positive neurons and their afferents from the FC all the way to the VTA/SNc. (**j**) Representative maximum projection image of GFP positive axons (green) labeled by retrograde lenti-FuGB2-Cre tracing from the VTA/SNc. Vglut1 and tyrosine hydroxylase immunohistochemistry labels dopamine-producing neurons (red) and presynaptic terminals (white). (**k**) High magnification view of co-localized axons (green), excitatory presynaptic marker (white) and dopamine neurons (red) within the VTA/SNc. All representative images were successfully repeated more than three times.

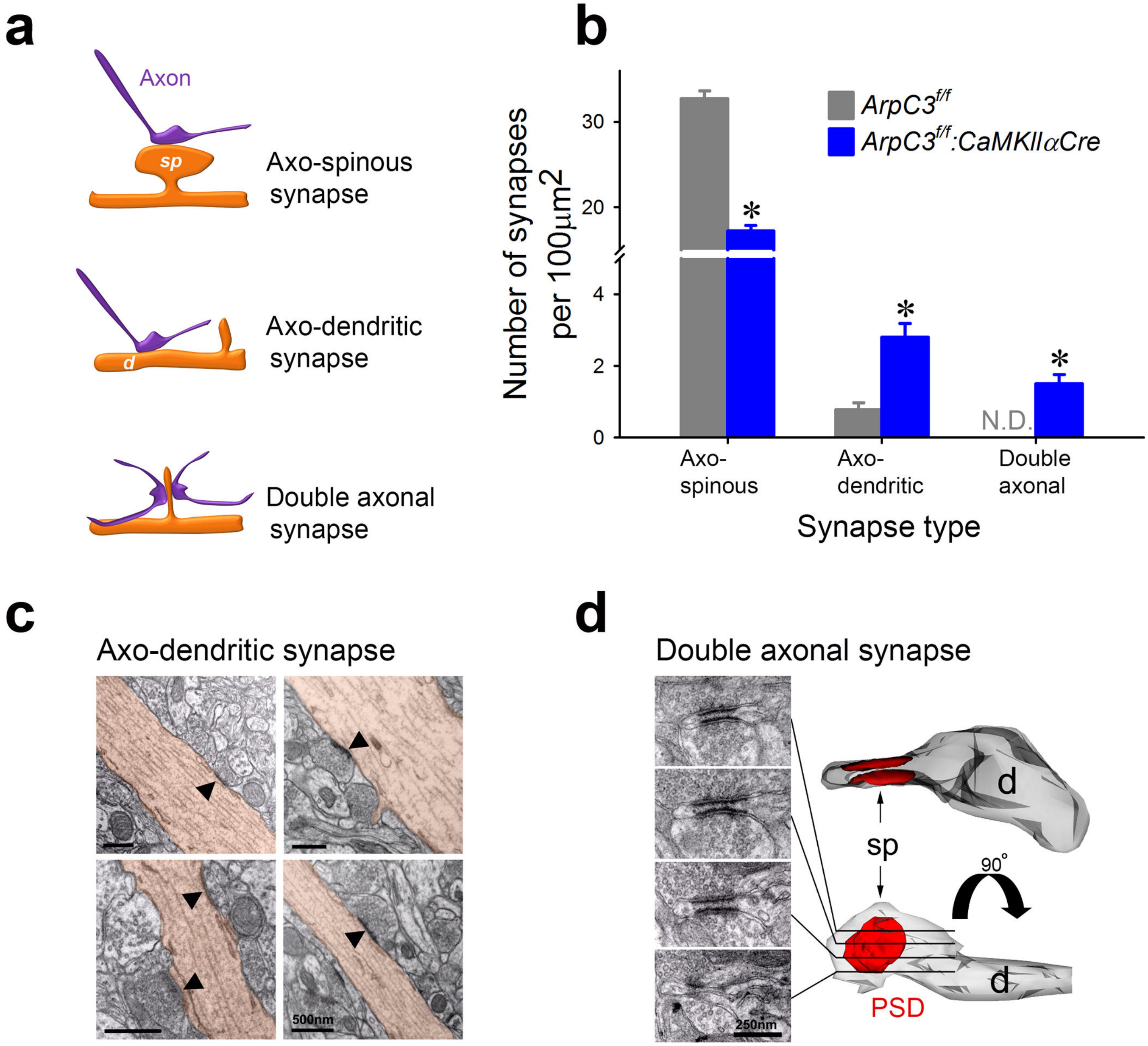

Fig. 4. Loss of Arp2/3 function leads to the formation of abnormal synaptic contacts

(**a**) Schematic illustrating three types of asymmetric synaptic contacts observed in the Arp2/3 mutant mice. (**b**) Graph showing mean numbers of three types of synapses in control (*ArpC3*$^{f/f}$; grey; n=70 micrographs from 3 mice) and cKO (*ArpC3*$^{f/f}$*:CaMKIIαCre*; blue; n=75 micrographs from 3 mice) mice (independent *t*-test, **p*<0.0001). (**c**) Electron micrographs of asymmetric synapses (marked by arrowheads) making direct contact with dendritic shafts (brown) in the frontal cortex of Arp2/3 mutant mice. (**d**) Serial electron micrographs (left) depicting an example of a reconstructed double axonal spine in the frontal cortex of Arp2/3 mutant mouse. sp; spine, d; dendrite, PSD; post-synaptic density. **ps*<0.0001. N.D.= not detected. Data are presented as mean ±SEM.

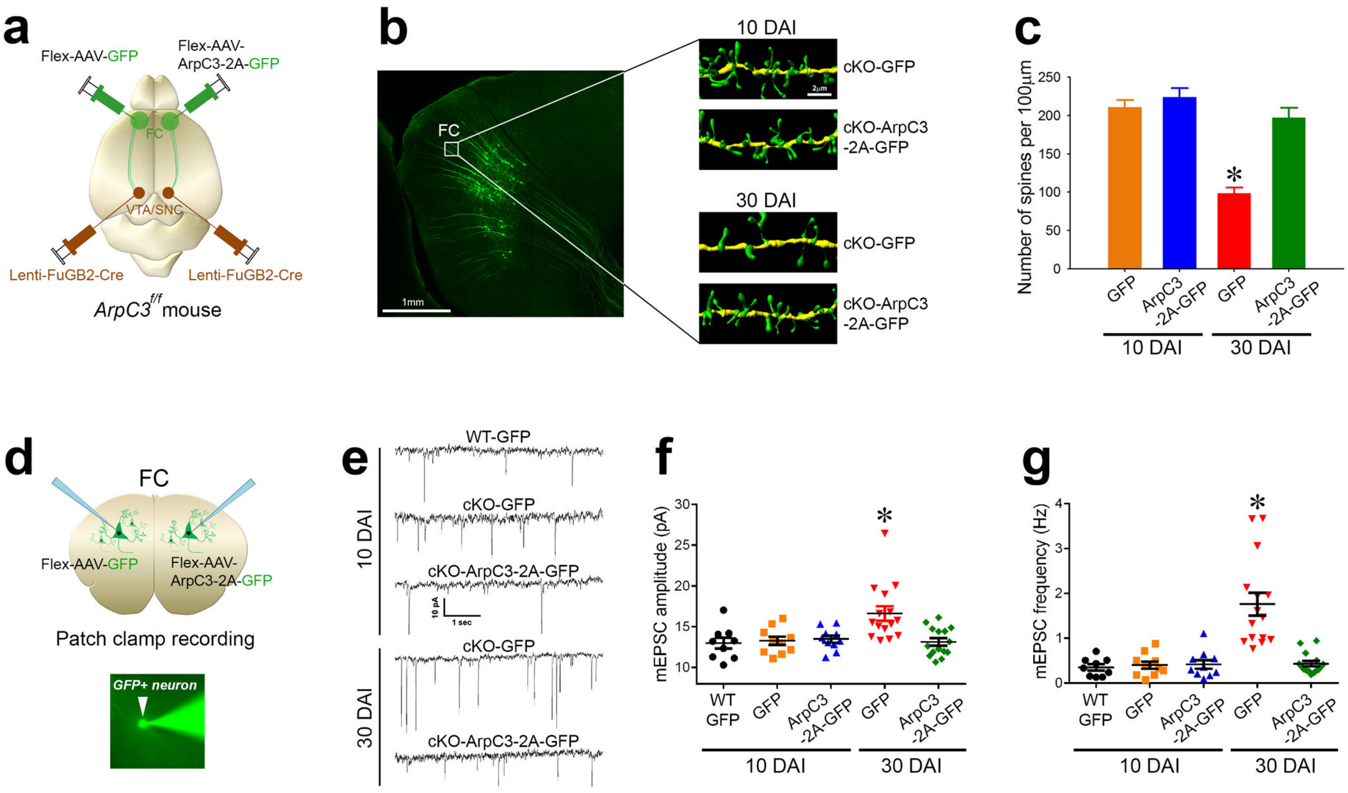

Fig. 5. Spine loss leads to excitation of the cortico-VTA/SNc circuit in Arp2/3 mutant mice

(**a**) Schematic representation of the labeling approach to generate cKO (Flex-AAV-GFP) versus rescue (Flex-AAV-ArpC3-2A-GFP) frontal cortical (FC) to VTA/SNc neurons. (**b**) Representative reconstructions from FC dendrites of cKO-GFP (control) versus cKO-ArpC3-2A-GFP (rescue) neurons at either 10 days after infection (top panels, 10 DAI) or 30 days after infection (bottom panels, 30 DAI). (**c**) Quantification of spine density after rescue, compared to control [n=16 (10 DAI-control; orange bar), n=14 (10 DAI-rescue; blue bar), n=19 (30 DAI-control; red bar), n=13 (30 DAI-rescue; green bar)] (*$p<0.0001$; two-way ANOVA followed by *post-hoc* tests). (**d**) Diagram depicting the patch clamp strategy from either GFP-positive neurons that are either control (cKO-GFP) or rescue hemisphere (cKO-ArpC3-2A-GFP) using the labeling strategy of (a). Representative image shows an Alexa Fluor®488 filled pipette patching onto a GFP-positive neuron (bottom panel). (**e**) Representative mEPSC traces of GFP-positive WT neurons, cKO neurons (cKO-GFP), or cKO neurons rescued with ArpC3 (cKO-ArpC3-2A-GFP). Top traces are from 10 DAI, bottom traces are from 30 DAI. (**f–g**) Box-and-Whisker graphs summarizing the mEPSC amplitude (f) and frequency (g). [n=9 (10 DAI-WT; black dots), n=10 (10 DAI-control; orange dots), n=10 (10 DAI-rescue; blue dots), n=15 (30 DAI-control; red dots), n=15 (30 DAI-rescue; green dots)] (*$ps<0.001$; two-way ANOVA followed by *post-hoc* tests). Data are presented as mean ±SEM.

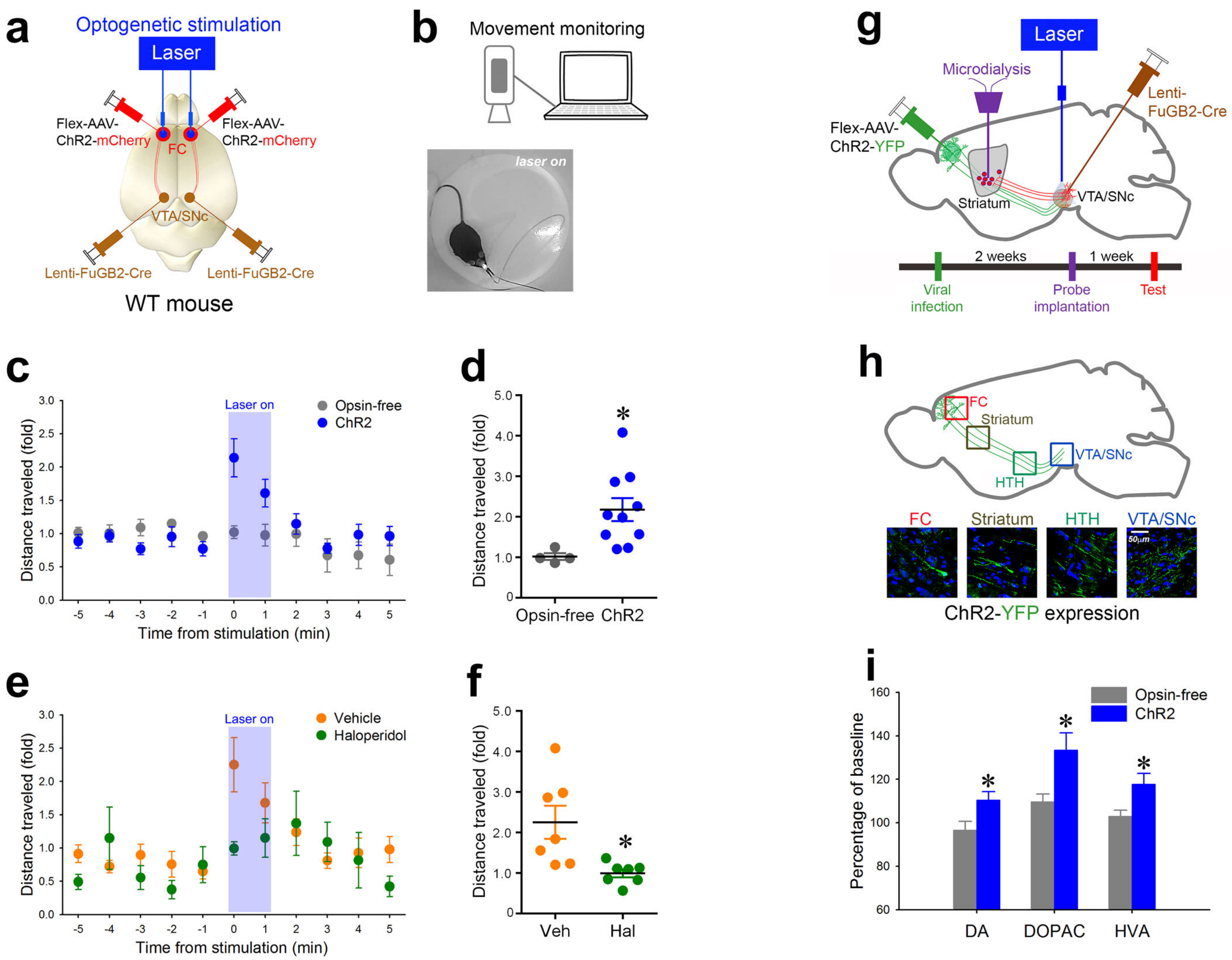

Fig. 6. Selective activation of the cortico-VTA/SNc circuit in wildtype mice stimulates haloperidol-sensitive locomotion and elevates dopamine within the striatum

(**a**) Schematic representation of the optogenetic stimulation strategy for activating the frontal cortical to VTA/SNc projections. (**b**) Representative schematic of the movement tracking system and image of an experimental mouse showing the onset of bilateral 473nm light stimulation. (**c**) Graph of distances moved (fold over baseline) over time in ChR2-expressing mice (blue circles; n=10) and in opsin-free-expressing control mice (gray circles; n=4). Blue area represents period of stimulation with 473nm light (10 ms pulse width, 30 Hz, 5 mW). (**d**) Distance moved (fold over baseline) in ChR2-expressing mice during the first minute of light stimulation (blue bar) versus that of opsin-free controls (grey bar) (independent *t*-test;**p*<0.05). (**e**) Graph of distance moved (fold over baseline) over time for WT mice treated with vehicle (orange circles) or 0.2mg/kg haloperidol (green circle). Blue area represents period of stimulation as in (c). (**f**) Distance moved (fold over baseline) during the first minute of light stimulation for vehicle (orange bar; n=7) versus haloperidol-treated (green bar; n=7) mice (independent *t*-test;**p*<0.05). (**g**) Schematic representation of the optogenetic stimulation strategy for stimulating the frontal cortical axons within the VTA/SNc while simultaneously measuring dopamine levels in the ventral striatum. Time schedule of the experiment is presented below. (**h**) Schematic representation (top panel) corresponding to the high magnification confocal images showing the expression of ChR2-YFP from the frontal cortex (FC) all the way to the VTA/SNc. HTH, hypothalamus. (**i**) Percent differences from baseline (monoamine levels before activation) of extracellular levels of striatal dopamine (DA) and its metabolites (DOPAC, HVA) after optogenetic stimulation (gray bar, opsin-free controls; n=10) (blue bar, ChR2; n=13) (independent *t*-test;**ps*<0.05). Data are presented as percent mean ±SEM.